Supporting Information for

How antisolvent induced ligand-stripping shapes $CsPbX_3$ nanocrystals and their assemblies

Jonas L. Hiller,[1] Robert Thalwitzer,[1] Ata Bozkurt,[1] Ross Ewan Carter,[2] Theresa Hettiger,[1] Markus Fröhlich,[1] Richard Hodak,[1] Matheus Gomes Ferreira,[3] Martin Eberle,[1] Ekaterina Kneschaurek,[2] Dmitry Lapkin,[2] Gerard Hinsley,[4] Bihan Wang,[4] Kuan Hoon Ngoi,[4] Elke Nadler,[1] Wojciech Roseker,[4] Fabian Westermeier,[4] Michael Sprung,[4] Dmitry Baranov,[3] Jannika Lauth,[1] Frank Schreiber,[2] Ivan A. Vartanyants,[4] Marcus Scheele[1]** and Ivan A. Zaluzhnyy[2]**

[1] Institute for Physical and Theoretical Chemistry, University of Tübingen, Auf der Morgenstelle 18, 72076 Tübingen, Germany

[2] Institute of Applied Physics, University of Tübingen, Auf der Morgenstelle 10, 72076, Tübingen, Germany

[3] Division of Chemical Physics and NanoLund, Department of Chemistry, Lund University, P.O. Box 124, SE-221 00 Lund, Sweden

[4] Deutsches Elektronen-Synchrotron DESY, Notkestraße 85, 22607 Hamburg, Germany

---

**Corresponding authors

SI Section 1 – Properties of the $CsPbBr_3$ NCs

1.1 $CsPbBr_3$ stock solution concentration

A series of dilutions of the $CsPbBr_3$ NC stock solution in hexane was created and the corresponding absorbance spectra recorded. The recorded extinction values at 335 nm and 400 nm, listed in Table S1, were used to calculate the concentration of the stock solution using the molar extinction coefficients from Maes *et al.*[1] according to eq. S1.

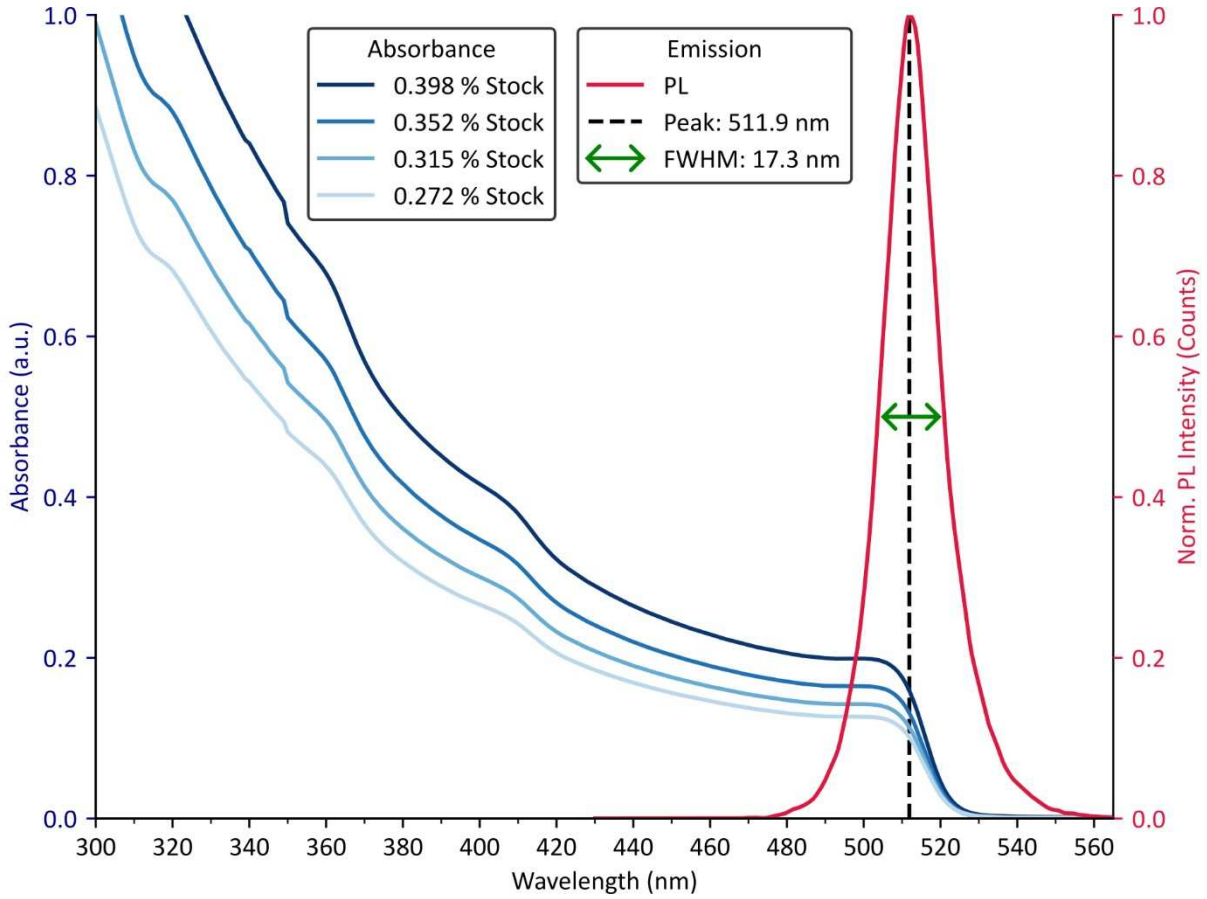

Figure S1. Norm. photoluminescence spectrum and absorbance measurements of a series of dilutions of the $CsPbBr_3$ NC stock solution in hexane. A hexane blank measurement was subtracted from all absorbance measurements. The measurements were performed in a quartz cuvette with a path length of 1 cm.

Table S1. Extinction values E_λ (λ = 335 nm and 400 nm) from absorbance measurements of a concentration series of the $CsPbBr_3$ stock solution displayed in Figure S1. The concentrations c_λ were calculated according to eq. S1.

Stock Volume Fraction f	$E_{335\,nm}$	$c_{335\,nm}$ **(µM)**	E_{400nm}	$c_{400\,nm}$ **(µM)**
0.398% (6 µl Stock + 1.5 ml Hexane)	0.879826	4.17824	0.416233	4.19293
0.352% (6 µl Stock + 1.7 ml Hexane)	0.742584	3.98733	0.347051	3.95288
0.315% (6 µl Stock + 1.9 ml Hexane)	0.647549	3.88545	0.300743	3.82779
0.272% (6 µl Stock + 2.1 ml Hexane)	0.572480	3.97806	0.266142	3.92291

$$c_\lambda = \frac{E_\lambda}{\varepsilon_\lambda(Lit.) \cdot f \cdot 1\,cm} \quad (S1)$$

1.2 $CsPbBr_3$ NC stock solution size distribution

Determination of the NC size distribution in the stock solution by scanning transmission electron microscopy is displayed in Fig. S2.

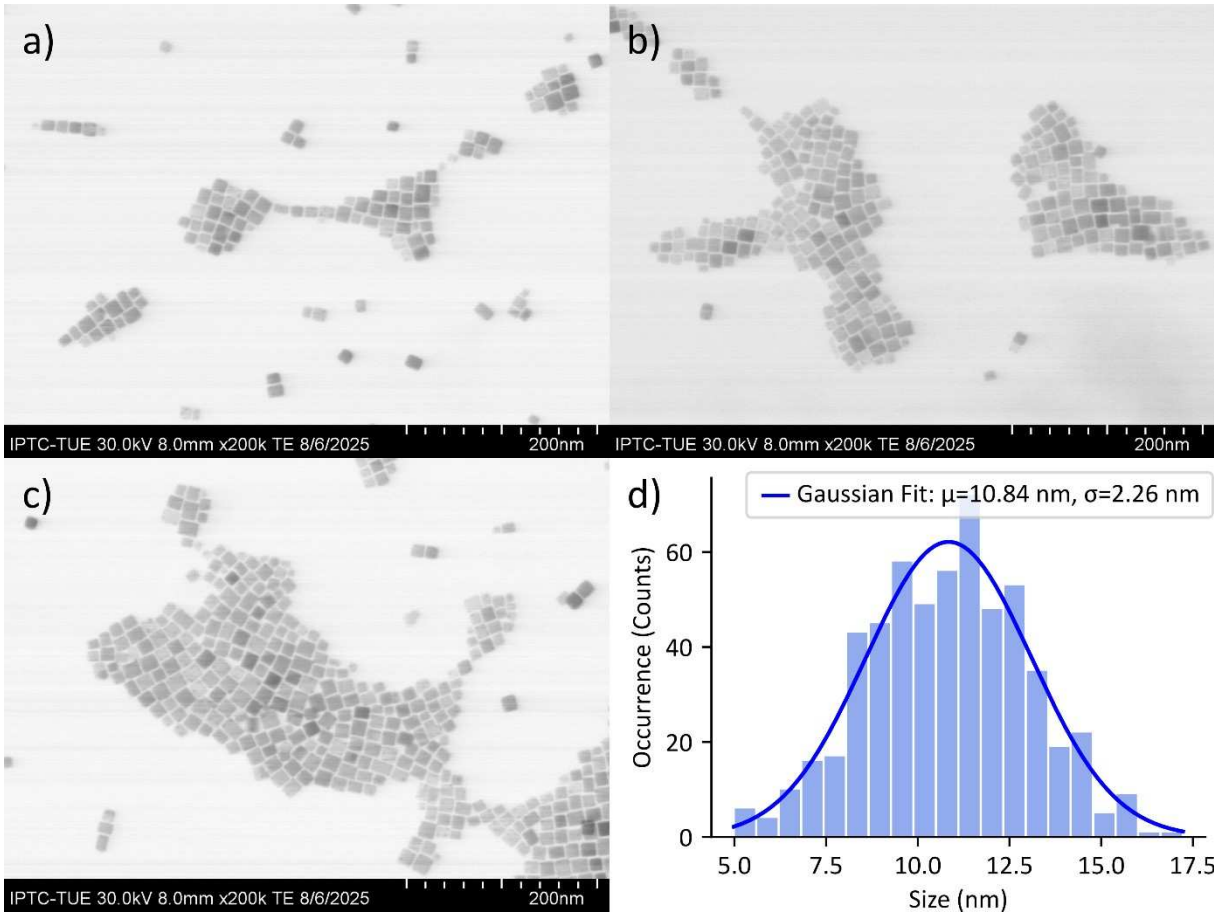

Figure S2. a-c) STEM images of $CsPbBr_3$ NCs dropcasted from the stock solution in hexane. d) Size distribution of the NCs in the stock solution from measuring the edge lengths of a total number of 571 NCs.

In this work, we used the same $CsPbBr_3$ stock solution that had been employed for the assembly of the SCs for the synchrotron experiments. Compared to the NC size distribution values reported in our previous study, which were recorded freshly after the synthesis of the stock solution, we see an increase of the average NC size from 7.5 to 10.8 nm and a broader size distribution.[2] We attribute these changes to aging of the stock solution, as, while stored in a glovebox, nearly two years elapsed between the two measurements.

1.3 Qualitative NMR of oleylamine and oleic acid

Fig. S3 displays ^{1}H-NMR spectra of the vinyl signals of OAM and OA in the $CsPbBr_3$ NC stock solution. Compared to the sharp vinyl signals of the pure ligands, the signals in the NC stock are broadened and shifted, which is a characteristic signature of surface-bound ligands.[3,4] We do not detect sharp signals corresponding to free OAM or OA in the NC stock solution, indicating that nearly all ligands are bound to NC surfaces.

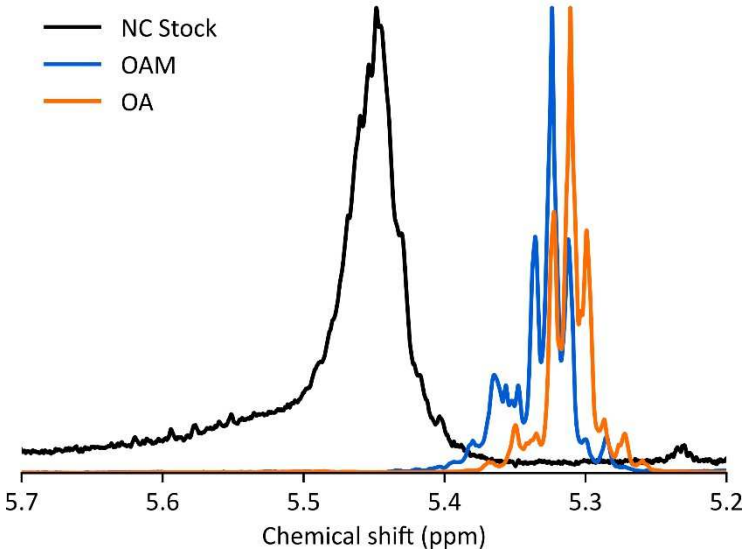

Figure S3. ^{1}H-NMR vinyl signals of the NC stock solution and free oleylamine and oleic acid recorded in toluene. The signals are normalized and serve as a qualitative reference.

1.4 Quantitative NMR

To quantify the loss of ligands during the two-layer phase diffusion assembly using acetonitrile antisolvent 400 µL of a 15 mM ethylene carbonate in d_6-DMSO solution was added to all investigated samples to decompose all NCs and release the surface-bound ligands. For the assembly process 500 µL of acetonitrile were overlayered with 100 µL of the 4 µM stock solution and additional 500 µL of hexane. Quantitative NMR was performed on four samples: The NC stock solution, from which we obtain the number of ligands/NC prior to the assembly, the residual acetonitrile remaining in the test tube after the assembly, the material adhered to the inner wall of the test tube, and finally the SCs from the crystallization substrate.

Table S2. Quantification of OAM/OA ligands in the samples taken from the two-layer phase diffusion assembly of $CsPbBr_3$ NCs. The corresponding vinyl proton signals are displayed in Figure 1e of the main text.

Sample	Vinyl ^{1}H Integrals I_A	Number of Ligands n_L(mol)	P (%)	P_{norm}(%)
Stock	0.2673	8.019e-7	100	100
Acetonitrile	0.1554	4.662e-7	58.14	51
Test Tube	0.1173	3.519e-7	43.88	38
SC Wafer	0.0328	0.984e-7	12.27	11

In Table S2, the molar amount of ligands n_L in each sample was calculated from the vinyl proton integrals I_A according to eq. S2:

$$n_L = n_{ST} \cdot \frac{I_A}{N_A} \quad (S2)$$

where:

n_{ST} = 6e-6 mol is the molar amount of the external standard (ethylene carbonate),

I_A is the integral of the OA/OAM vinyl proton signals of the sample,

N_A = 2 is the number of protons contributing to the OA/OAM vinyl proton signals,

P is the percentage of ligands recovered from the individual samples with respect to the number of ligands in the stock solution. P_{norm} represents the same values normalized so that the total ligand recovery equals 100%.

The average number of ligands per nanocrystal $n_{L/NC}$ for the different samples is then calculated according to eq. S3:

$$n_{L/NC} = \frac{n_L}{V_{NC} \cdot c_{NC} \cdot f_{NC}} \quad (S3)$$

where $V_{NC} = 100\ \mu L$ is the volume of the stock solution used in the assembly, $c_{NC} = 4\ \mu M$ is the NC concentration in the stock solution (calculated from the values listed in Table S1), and f_{NC} is the fraction of the NCs added to the assembly that are present in each sample.

For the stock solution, f_{NC} = 1 by definition and $n_{L/NC}$ can be directly calculated. To calculate $n_{L/NC}$ for the crystallization substrate, the f_{NC} value corresponding to the fraction of NCs that deposit on the substrate need to be estimated. The complementary fraction corresponds to NCs adhered to the inner wall of the test tube. Since no NCs were detected in the residual acetonitrile phase, these fractions sum to unity. A photograph of the test tube after the two-layer phase diffusion assembly is depicted in Fig. S4.

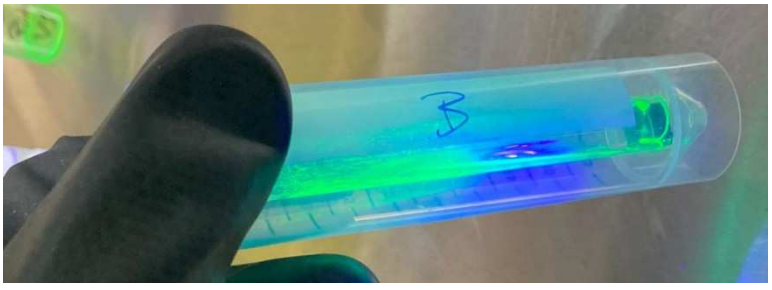

Figure S4. Photograph of the test tube after the two-layer phase diffusion assembly using acetonitrile antisolvent, showing NCs both adhered to the inner wall of the test tube and deposited on the Si substrate at the bottom of the test tube (right side of this rotated image). The residual acetonitrile phase was removed prior to the photograph.

From our observations, we estimate that approximately half of the NCs in the stock solution are deposited on the crystallization substrate, corresponding to a ligand coverage 492 ligands/NC. As a lower bound, assuming only 25 % of the NCs are deposited on the substrate, yields a coverage of 984 ligands/NC. As an upper bound, a 75 % substrate fraction results in a coverage of 328 ligands/NC.

1.5 Further information on NC self-assembly

The NCs display a pronounced tendency towards self-assembly. When spin-coated from the stock solution in hexane, they typically do not form homogenous NC films but instead organize into small SCs with lateral dimensions of approx. 1x1 μm^2. This is displayed in Fig. S5.

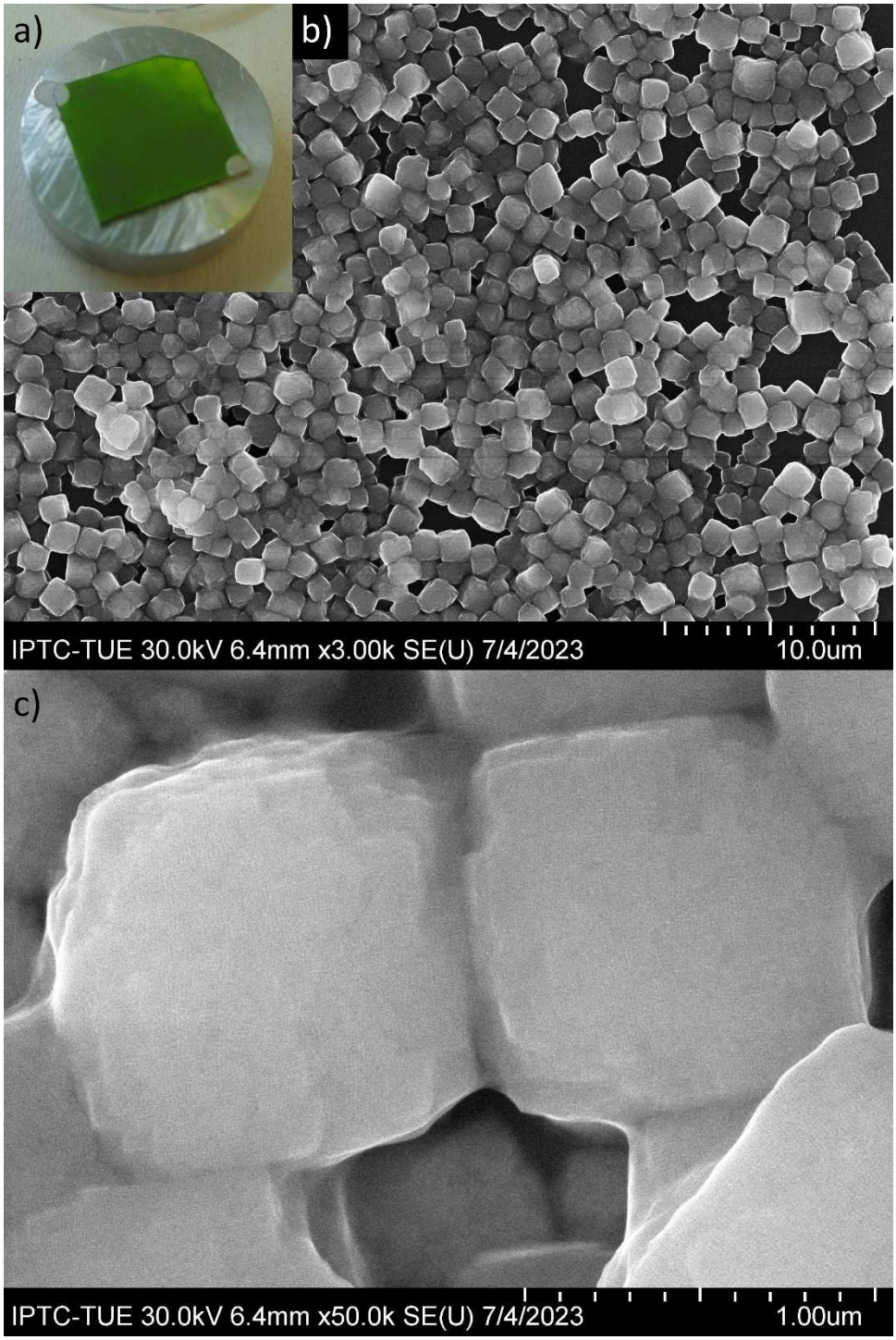

Figure S5. a) Photograph of the Si wafer spin-coated with $CsPbBr_3$ NCs from the stock solution in hexane. b) SEM image of the Si wafer in a), displaying the formation of small SCs. c) High-resolution close-up SEM image, displaying the high degree of order of the constituent NCs in the small SCs.

Compared to solvent evaporation driven self-assembly, the two-layer phase diffusion assembly using acetonitrile antisolvent yields larger and much thicker SCs. Using this assembly, terrace-like height increases are often observed at the very edges of the SCs as shown in Fig. S6.

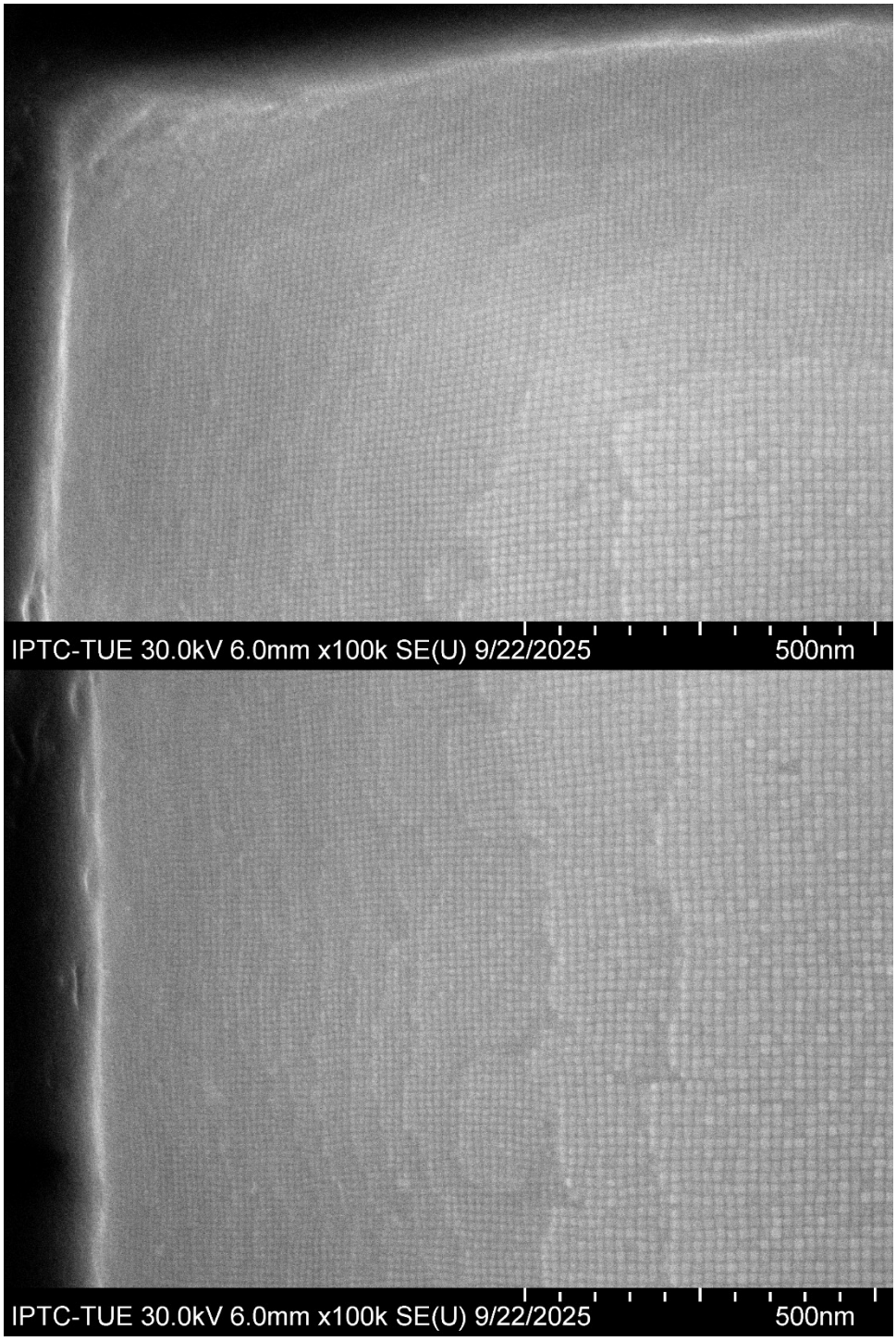

Figure S6. Terrace-like height steps at the edges of $CsPbBr_3$ SCs obtained via the two-layer phase diffusion assembly using acetonitrile antisolvent. The radial NC size gradient with increasingly smaller NCs towards the SC edges is clearly visible.

The SCs obtained from the two-layer phase diffusion assembly using acetonitrile antisolvent are not completely isolated but embedded within a NC film. As displayed in Fig. S7, this film surrounding the SCs is not completely disordered but consists of domains exhibiting high orientational order.

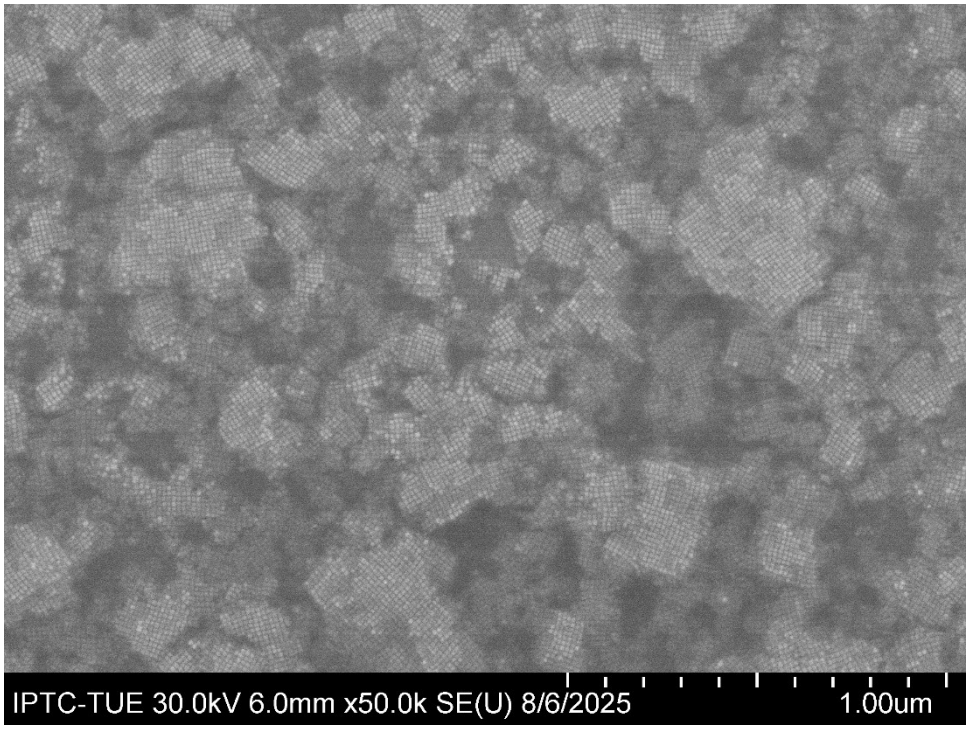

Figure S7. High-resolution SEM image of the film region surrounding the $CsPbBr_3$ SCs obtained from the two-layer phase diffusion assembly using acetonitrile antisolvent.

SI Section 2 - X-ray nanodiffraction in transmission geometry

A comprehensive description of the general workflow used to evaluate the X-ray nanodiffraction data recorded in transmission geometry can be found in the Supporting Information of our previous work.[2] The following section focuses on addressing the specifics of the WAXS data presented in the present work.

2.1 Separation of contributions to azimuthal broadening

The measured, total azimuthal peak width (fwhm) $\Delta\phi_m$ contains contributions from orientational disorder $\Delta\phi_{do}$, the finite crystallite size $\Delta\phi_s$, and microstrain $\Delta\phi_\varepsilon$. For the assumption of Gaussian line shapes, these independent broadening mechanisms add in quadrature. The azimuthal peak broadening due to disorder is calculated according to eq. S4.

$$\Delta\phi_{do} = \sqrt{\Delta\phi_m^2 - \Delta\phi_s^2 - \Delta\phi_\varepsilon^2} \quad (S4)$$

Finite size broadening is isotropic and contributes equally to both the radial and azimuthal peak width. In reciprocal space, the radial size broadening Δq_s is calculated according to eq. S5, where K = 0.85 is the shape factor and s is the NC size, obtained from WH analysis for all positions on the SC (Fig. 2e of the main text).

$$\Delta q_s = \left(\frac{2\pi \cdot K}{s} \right) \quad (S5)$$

This radial broadening can be translated into azimuthal broadening due to finite NC size $\Delta\phi_s$ according to eq. S6 by considering Δq_s as the arc length on the diffraction ring at q_0.

$$\Delta\phi_s = \left(\frac{\Delta q_s}{q_0} \right) = \left(\frac{2\pi \cdot K}{s \cdot q_0} \right) \quad (S\wedge 6)$$

The microstrain parameter ε obtained from WH analysis for all positions on the SC (Fig. 2e of the main text) is dimensionless and quantifies the distribution of lattice spacings within the nanocrystals. It corresponds to the relative fwhm broadening per unit q. The actual radial peak broadening in reciprocal space due to microstrain is therefore calculated according to eq. S7.

$$\Delta q_\varepsilon = \varepsilon \cdot q_0 \quad (S\wedge 7)$$

The associated azimuthal broadening contribution due to microstrain is then calculated according to eq. S8 and is numerically equal to the WH derived microstrain parameter ε itself.

$$\Delta\phi_\varepsilon = \left(\frac{\Delta q_\varepsilon}{q_0} \right) = \varepsilon \quad (S\wedge 8)$$

Substituting equations S6 and S8 into S4, the azimuthal broadening due to disorder can be calculated directly from maps of $\Delta\phi_m$, s, and ε.

2.2 Calculations of the in-plane atomic lattice parameters

The pseudo-cubic atomic lattice parameter a can be directly calculated from the 100_{AL} reflection according to eq. S9.

$$a = \frac{2\pi}{q_0(100_{AL})} \quad (S9)$$

To calculate the pseudo-cubic atomic lattice parameter b according to eq. S10, the radial positions of both the 100_{AL} and 100_{AL} peaks are required.

$$b = \frac{2\pi \cdot a}{\sqrt{a^2 \cdot q_0^2(110_{AL}) - 4\pi^2}} \quad (S10)$$

The out-of-plane lattice parameter c cannot be determined from the dataset recorded in transmission geometry as all recorded atomic lattice reflexes have l=0 and therefore do not probe the out of plane spacing. It's calculation from diffraction data in reflection geometry is discussed in SI Section 3.

2.3 Calculation of the average SC lattice parameter

The lattice parameter of the SC $\langle a_{SC} \rangle$ is calculated according to eq. S11, where $\langle q_0 \rangle$ is the average q_0-value of the four first-order SAXS peaks and γ is the angle between the unit vector of the SC unit cell. γ is calculated according to eq. S.12, from the azimuthal peak positions (ϕ_0) of the four first-order SAXS peaks.

$$\langle a_{SC} \rangle = \frac{2\pi}{\langle q_0 \rangle \cdot \sin(\gamma)} \quad (S11)$$

$$\gamma = \frac{1}{2}\left(\phi_0^{001_{SC}} + \phi_0^{00\acute{1}_{SC}} - \pi\right) - \frac{1}{2}\left(\phi_0^{010_{SC}} + \phi_0^{0\acute{1}0_{SC}} - \pi\right) \quad (S12)$$

2.4 Instrumental resolution

The magnitude of the wave vector q is related to the half-scattering angle θ according to eq. S13, where λ = 0.9537 Å is the X-ray wavelength, and θ is the half scattering angle.

$$q = \frac{4\pi}{\lambda} \cdot \sin(\theta) \quad (S13)$$

The variation in q with respect to the half scattering angle is obtained by differentiation and is given in eq. S14.

$$\frac{dq}{d\theta} = \frac{4\pi}{\lambda} \cdot \cos(\theta) \quad (S14)$$

In transmission geometry with a 2D detector at distance L behind the sample, the half scattering angle can be calculated for any point on the detector at a real-space radial distance R from the direct beam according to eq. S15.

$$\theta = \frac{1}{2} \cdot \arctan\left(\frac{R}{L}\right) \quad (S15)$$

Differentiating eq. S15 with respect to R, we obtain the relation shown in eq. S16.

$$\frac{d\theta}{dR} = \frac{L}{2(L^2 + R^2)} \quad (S16)$$

Substituting eq. S16 into eq. S14 we can calculate the instrumental resolution in q-space Δq according to the relation in eq. S17, where the pixel size ΔP is the smallest resolvable step in R.

$$\Delta q = \frac{4\pi}{\lambda} \cdot \cos(\theta) \cdot \frac{L}{2(L^2 + R^2)} \cdot \Delta P \quad (S17)$$

Performing the calculation for L = 400 mm, ΔP = 75 µm, λ = 13 keV = 0.9537 Å at $q_0(100_{AL})$ = 1.072 Å^{-1}, the obtained value for the instrumental resolution is Δq = 0.0012 Å.

As displayed in Fig. S8, the changes in the radial positions of the atomic lattice reflections are discernibly even by eye in the raw diffraction patterns recorded from the edges and the center of the SC.

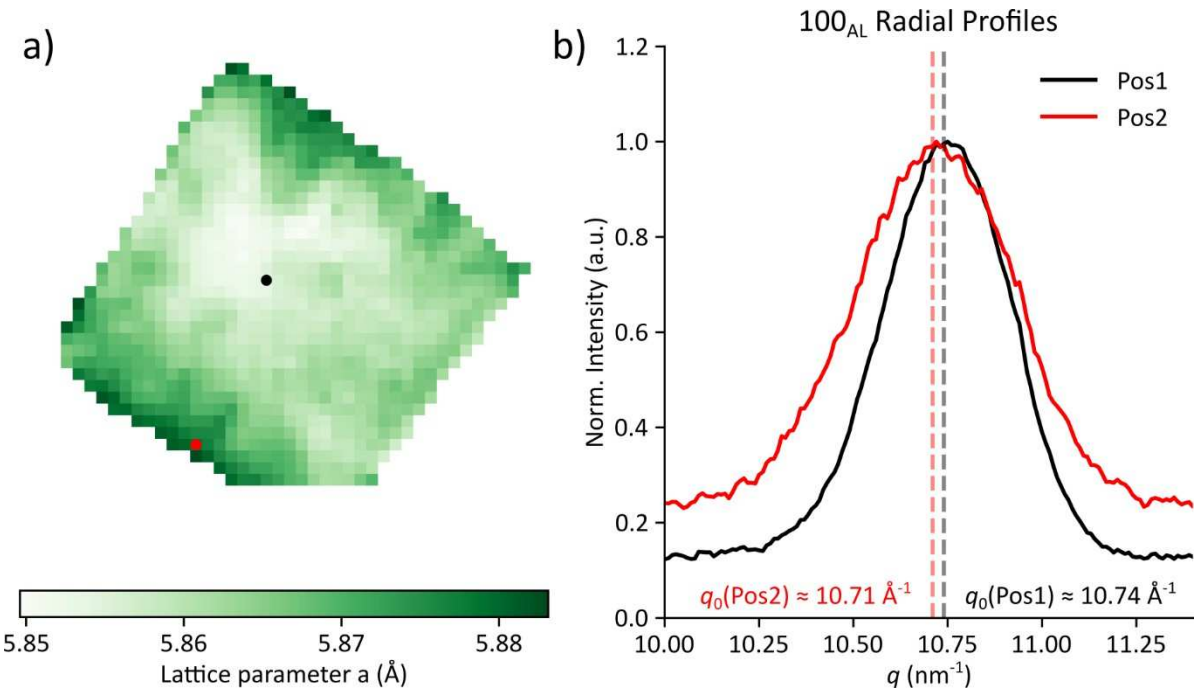

Figure S8. a) Map of the lattice parameter a of the $CsPbBr_3$ SC from Fig.3 of the main text, directly calculated from $q_0(100_{AL})$. b) Raw, unfitted radial profiles of the 100_{AL} reflection recorded from the positions indicated in a) at the center of the SC (Pos1 - black) and at the SC edge (Pos2 - red). The differences in NC size between the center and the edge are evident from the radial peak broadness.

2.4 Spatially-resolved in-plane atomic lattice parameters of a $CsPbBr_2Cl$ and a $CsPbCl_3$ SC

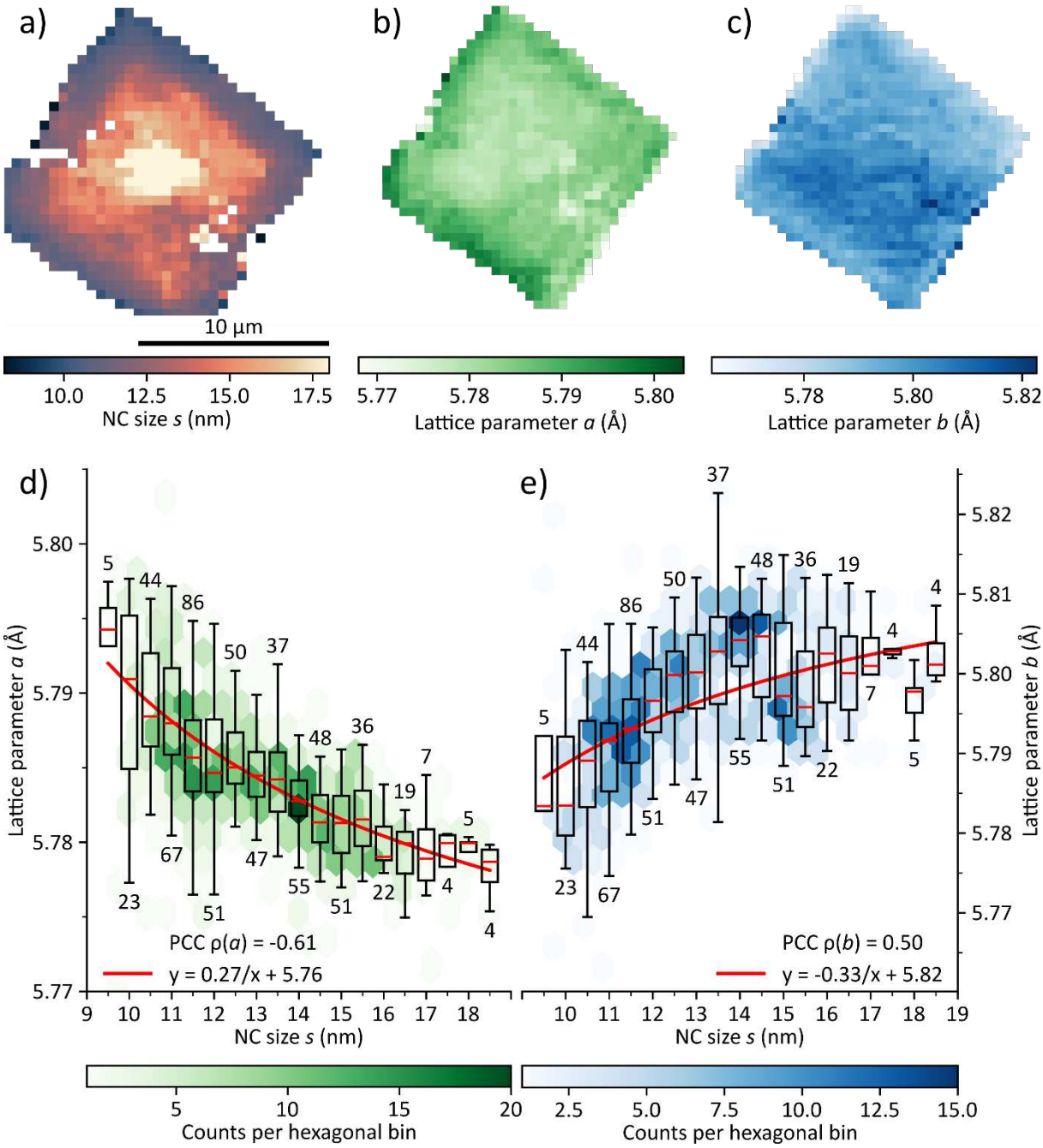

Figure S9. In-plane lattice spacing of a $CsPbBr_2Cl$ SC. a) Map of the NC size s obtained from WH analysis. b) Map of the pseudo-cubic lattice parameter a. b) Map of the pseudo-cubic lattice parameter b. d), e) Correlation of lattice parameters a and b with NC size, respectively. Hexagonal binning displays the statistical distribution, while boxplots indicating the spread and median value within each 0.5 nm size interval. Numbers attached to the boxplots denote the number of pixels contributing to the respective NC size bins. The Pearson correlation coefficients (PCC) ρ are stated to quantify the degree of linear correlation. The median values of the boxplots are fitted using an inverse proportionality with an offset.

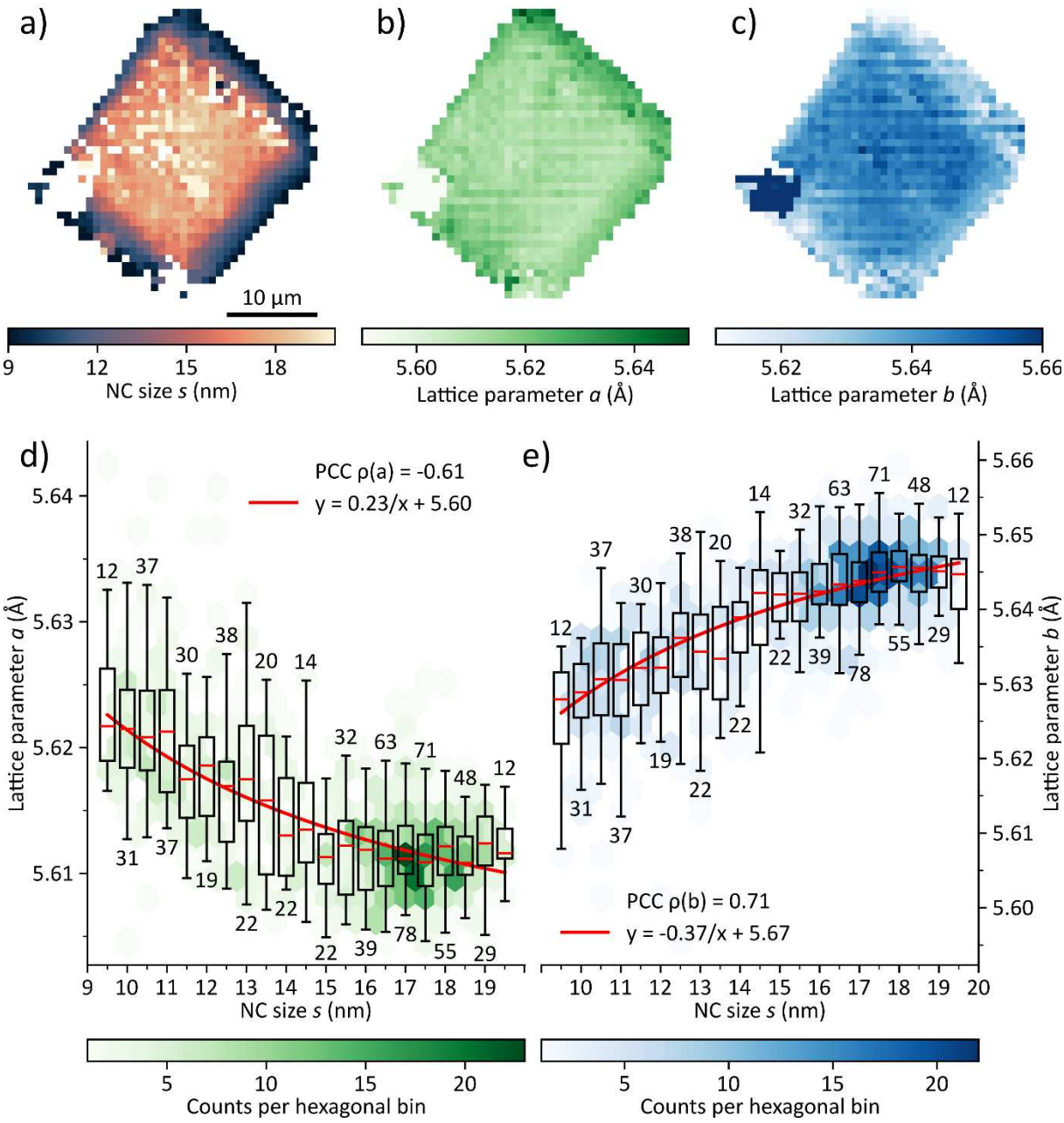

Figure S10. In-plane lattice spacing of a $CsPbCl_3$ SC. a) Map of the NC size s obtained from WH analysis. b) Map of the pseudo-cubic lattice parameter a. b) Map of the pseudo-cubic lattice parameter b. d), e) Correlation of lattice parameters a and b with NC size, respectively. Hexagonal binning displays the statistical distribution, while boxplots indicating the spread and median value within each 0.5 nm size interval. Numbers attached to the boxplots denote the number of pixels contributing to the respective NC size bins. The Pearson correlation coefficients (PCC) ρ are stated to quantify the degree of linear correlation. The median values of the boxplots are fitted using an inverse proportionality with an offset.

SI Section 3 – X-ray characterization of as-synthesized $CsPbBr_3$ nanocrystals

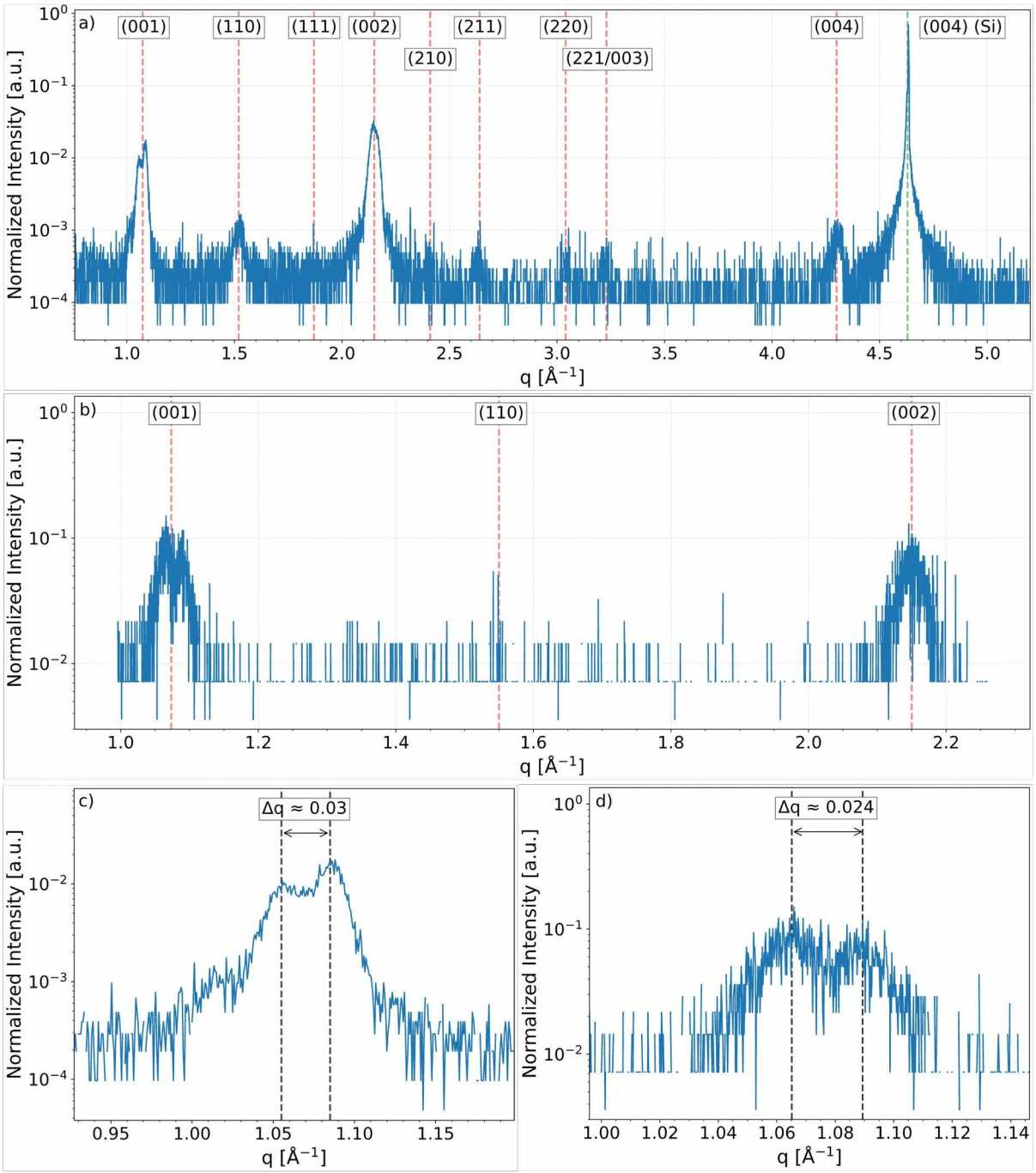

Fig. S11. X-ray diffraction intensity curves of a) dropcast and b) spin coated $CsPbBr_3$ nanocrystals on Si substrates, and c,d) magnified regions around the respective first-order Bragg peaks. Both profiles were measured in θ:2θ reflection geometry. The Bragg peaks of $CsPbBr_3$ are labelled by red dashed lines using cubic notation. The green dashed line denotes the (004) Bragg peak from the silicon substrate. Black dashed lines show the centre of mass for each interference fringe of the split first-order Bragg peak.

We characterized the dropcast and spin-coated $CsPbBr_3$ nanocrystals prior to acetonitrile exposure using the laboratory diffractometer (GE-3303TT, Cu-$K_{\alpha 1}$ radiation) in θ:2θ reflection geometry between the angles $\theta = 0 - 48\,°$, under ambient conditions. Fig. S11a) shows the region $5.5\,° \leq \theta \leq 39.5\,°$ of this measurement for a sample prepared via dropcasting and Fig. S11b) shows the region $7\,° \leq \theta \leq 16\,°$ for a sample prepared using

spin coating techniques. Due to the large beam size, this measurement represents the scattered intensity averaged over all SCs present on the film.

While we acknowledge that there can be difficulties in differentiating between cubic and orthorhombic phases in $CsPbBr_3$ nanocrystals (especially when the signal to noise ratio is high as is found in this measurement), we argue that the measured intensity curve is more consistent with that of a cubic structure, because the position of diffraction peaks align with a cubic structure and no splitting of the peaks is visible, which would indicate deviations of the lattice from a cubic symmetry. The only exception is the split of the (001) peak (see Fig. S11c)-d)). However, we argue that this split originates from the interference of the scattering signal by neighbouring nanocrystals within the superlattice and not from the orthorhombic structure of the nanocrystals.

Previous investigations into the same phenomena show that first-order Bragg peak splitting occurs in a highly ordered cubic NCs as a result of the periodicity of the precisely spaced superlattices within the SC.[5,6] In this case, the X-rays diffracted from the atomic lattice of neighbouring NCs interfere with each other, which results in an apparent splitting of an intrinsically broad first-order Bragg peak from individual NCs. Notably, due to the structural incoherence of the superlattice, there is no splitting expected for the higher order reflections, which is consistent with our data.

Figs. S11c) and d) provide clearer views of the first-order Bragg peak for both preparation methods. We compare the expected peak splitting due to superlattice periodicity to that of the measured value. Assuming an average centre-to-centre distance between NCs of approximately $\Lambda \approx 170\,\text{Å}$ (as shown in Fig. 4d) we can calculate an estimate of the expected peak splitting $\Delta q = 2\pi/\Lambda = 0.03695\,\text{Å}^{-1}$. This is on the same order of magnitude as the measured value for both dropcast ($\Delta q = 0.03\,\text{Å}^{-1}$) and spin-coated samples ($\Delta q = 0.024\,\text{Å}^{-1}$).

Finally, considering the spin-coated sample in particular, previous work[7–9] observes how $CsBrX_3$ nanoparticles crystalize in cubic phase, and notably not orthorhombic phase. They note that this is a stable state even during long exposure to air and ascribe the retention of cubic structure to high-temperature synthesis techniques and surface energy effects stemming from the quantum confinement of nanoparticles. More specifically, the increased band gap energies due to this confinement lead directly to the stabilization of the cubic phase. In conclusion, we are confident that our $CsPbBr_3$ samples show cubic, and not orthorhombic, structure.

SI Section 4 – Additional Spectroscopy Data

4.1 Quantum yields

Quantum yields were measured in solution using an integration sphere mounted in a UV-VIS-NIR spectrometer (Cary 5000, Agilent Technologies).

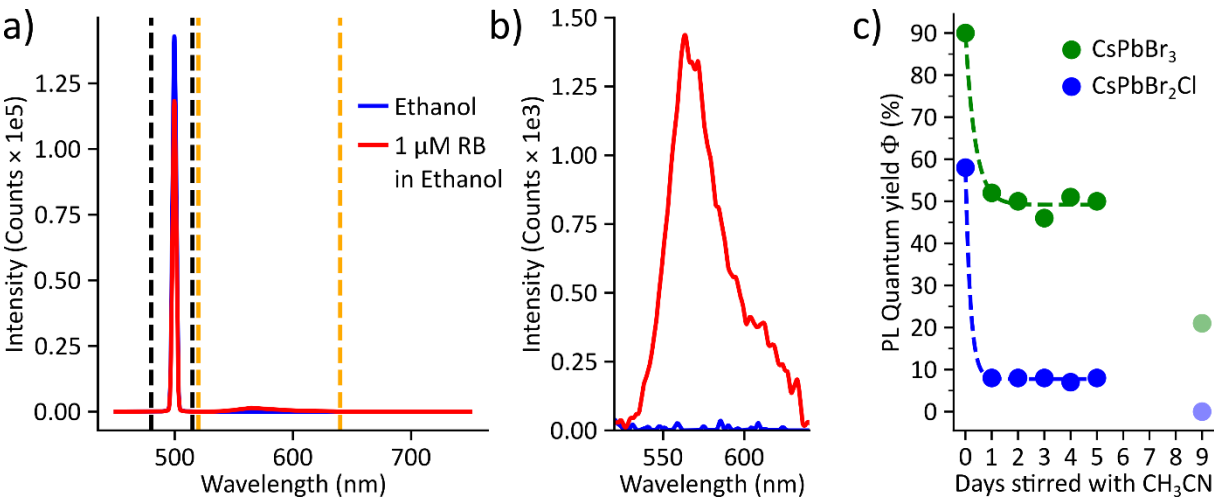

Figure S12. a) Spectra of a 1 µM solution of Rhodamine B in ethanol and the corresponding solvent blank recorded using an integrating sphere as a reference measurement. The excitation (black dashed lines) and emission (orange dashed lines) regions used for integration are indicated. b) Zoom on the emission region. c) Quantum yield measurements performed on $CsPbBr_3$ and $CsPbBr_2Cl$ NCs stirred with acetonitrile antisolvent for different durations.

Fig. S12a) and b) display a reference measurement of a 1 µM solution of Rhodamine B in ethanol excited at 500 nm. As indicated by the dashed lines in Fig. S12a), the excitation and emission regions were defined between 480 – 515 nm and 520 – 640 nm, respectively. The PL quantum yield Φ was calculated according to eq. S18, where I_{ex} and I_{em} denote the excitation and emission intensities, integrated over the respective wavelength ranges.

$$\Phi = \frac{\left(I_{em}(Sample) - I_{em}(Blank)\right)}{\left(I_{ex}(Blank) - I_{ex}(Sample)\right)} \cdot 100\,\% \qquad (S18)$$

The calculated PL quantum yield of Rhodamine B in ethanol was 64.6 %, in good agreement with literature values for this system.[10]

Fig. S12c) shows PL quantum yields measured for $CsPbBr_3$ and $CsPbBr_2Cl$ NCs stirred with acetonitrile antisolvent as a function of stirring time. Inside a glovebox, vials with stir bars were prepared by overlayering 3 mL of acetonitrile with 40 µL of the NC stock solutions in hexane plus an additional 3 mL of hexane. The vial contents were stirred inside the glovebox to ensure mixing of the two phases. Aliquots were taken approximately every 24 hours for PL quantum yield measurements for the first 5 days. Another data point was

acquired after 9 days of stirring. The time point 0 corresponds to the NC stock solutions measured prior to contact with acetonitrile.

A pronounced decrease of the PL quantum yield was observed for both halide compositions within the first 24 hours of stirring with acetonitrile. Specifically, the QY of $CsPbBr_3$ NCs decreased from approx. 90% to around 50%, while $CsPbBr_2Cl$ NCs displayed an even steeper drop of the QY from roughly 60% QY to around 9%. Over the following 5 days, the QY values remained largely constant. However, the dispersions became progressively more turbid, indicating a reduced colloidal stability due to ligand-stripping. After 9 days of stirring with acetonitrile $CsPbBr_3$ NCs only displayed around 20 % QY, whereas no photoluminescence could be recorded from the $CsPbBr_2Cl$ NCs.

4.2 TA Spectroscopy

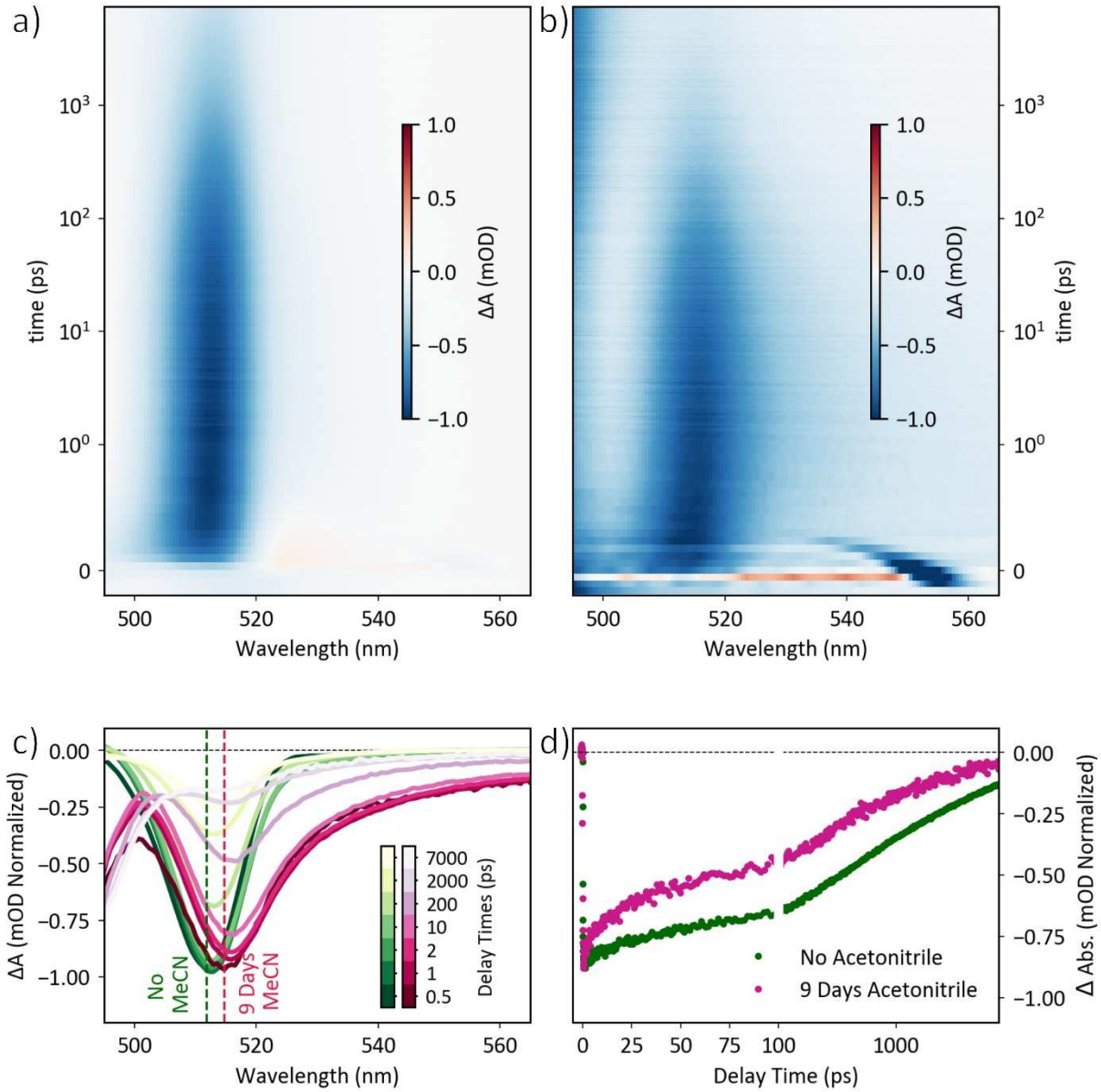

Figure S13: TA hyperspectra of $CsPbBr_3$ NCs dispersed in hexane before (a) and after (b) 9 days exposure to acetonitrile. c) Spectral line cuts of both samples showcasing redshift and broadening. d) Decay traces along the dashed lines in c) showing a faster decay for the exposed sample.

4.3 Fluorescence lineshape analysis

Fluorescence lineshape analysis of the spatially-resolved emission spectra presented in Fig. 4 of the main text was performed by fitting each spectrum with a Voigt profile as implemented in scipy.special.voigt_profile (SciPy version: 1.15.2, Python version: 3.12.3). This function evaluates the exact convolution of Gaussian and Lorentzian lineshapes through the Faddeeva function.

The extracted σ (the Gaussian standard deviation) and γ (Lorentzian half-width at half-maximum) parameters describe the homogeneous and inhomogeneous broadening contributions, respectively. The Voigt full width at half maximum $FWHM_V$ is approximated using eq. S18, with the Lorentzian FWHM $FWHM_L = 2\gamma$ and the Gaussian FWHM $FWHM_G = 2.3548\,\sigma$.[11]

$$FWHM_V = 0.5364 \cdot FWHM_L + \sqrt{0.2166 \cdot FWHM_L^2 + FWHM_G^2} \quad (S19)$$

To quantify the dominant broadening mechanism, fractional Gaussian and Lorentzian contributions to the overall Voigt profile were estimated by calculating the weighting parameter η according to eq. S20.[12] Here, $\eta = 0$ corresponds to a purely Gaussian and $\eta = 1$ to a purely Lorentzian lineshape.

$$\eta = 1.36603 \cdot \frac{FWHM_L}{FWHM_V} - 0.47719 \cdot \left(\frac{FWHM_L}{FWHM_V}\right)^2 + 0.11116 \cdot \left(\frac{FWHM_L}{FWHM_V}\right)^3 \quad (S20)$$

Fig. S14c) shows exemplary Voigt fits of the three select positions from Fig. 4 of the main text. Table S3 displays the extracted parameters.

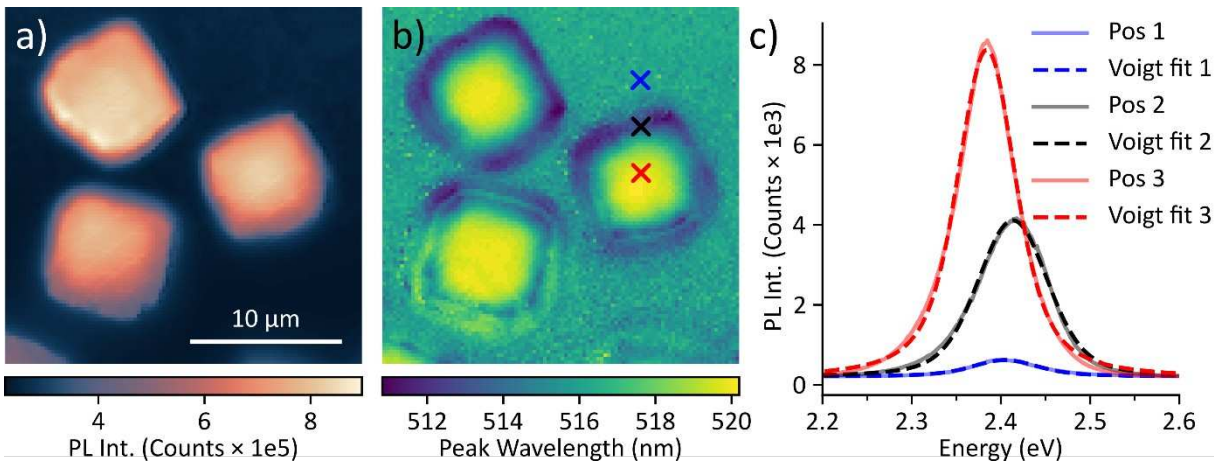

Figure S14. Spatially-resolved optical properties of $CsPbBr_3$ SCs obtained from the two-layer phase diffusion assembly using acetonitrile antisolvent. a) Map of the PL intensity. b) Map of the peak emission wavelength. c) Voigt fits of the PL spectra corresponding to the positions marked in b), located outside the SC (blue), at its edge (black), and at its center (red).

Table S3. Parameters extracted from the Voigt fit of the three spectra in Fig. S14 c).

Spectrum	Gaussian Contrib. (%)	Lorentzian Contrib. (%)	σ(eV)	γ(eV)
Pos1 (NC film)	38	62	0.02499	0.02393
Pos2 (SC edge)	60	40	0.03221	0.01541
Pos3 (SC center)	36	64	0.02154	0.02214

The spectra recorded from Pos1 in the NC film and from Pos3 at the SC center are both predominantly Lorentzian in shape. In contrast, the spectrum recorded from Pos2 at the SC edge exhibits a predominantly Gaussian lineshape. To verify whether this is representative of the entire mapped region, lineshape analysis was performed for each spectrum of the spectral map. The resulting parameter maps are displayed in Fig. S15.

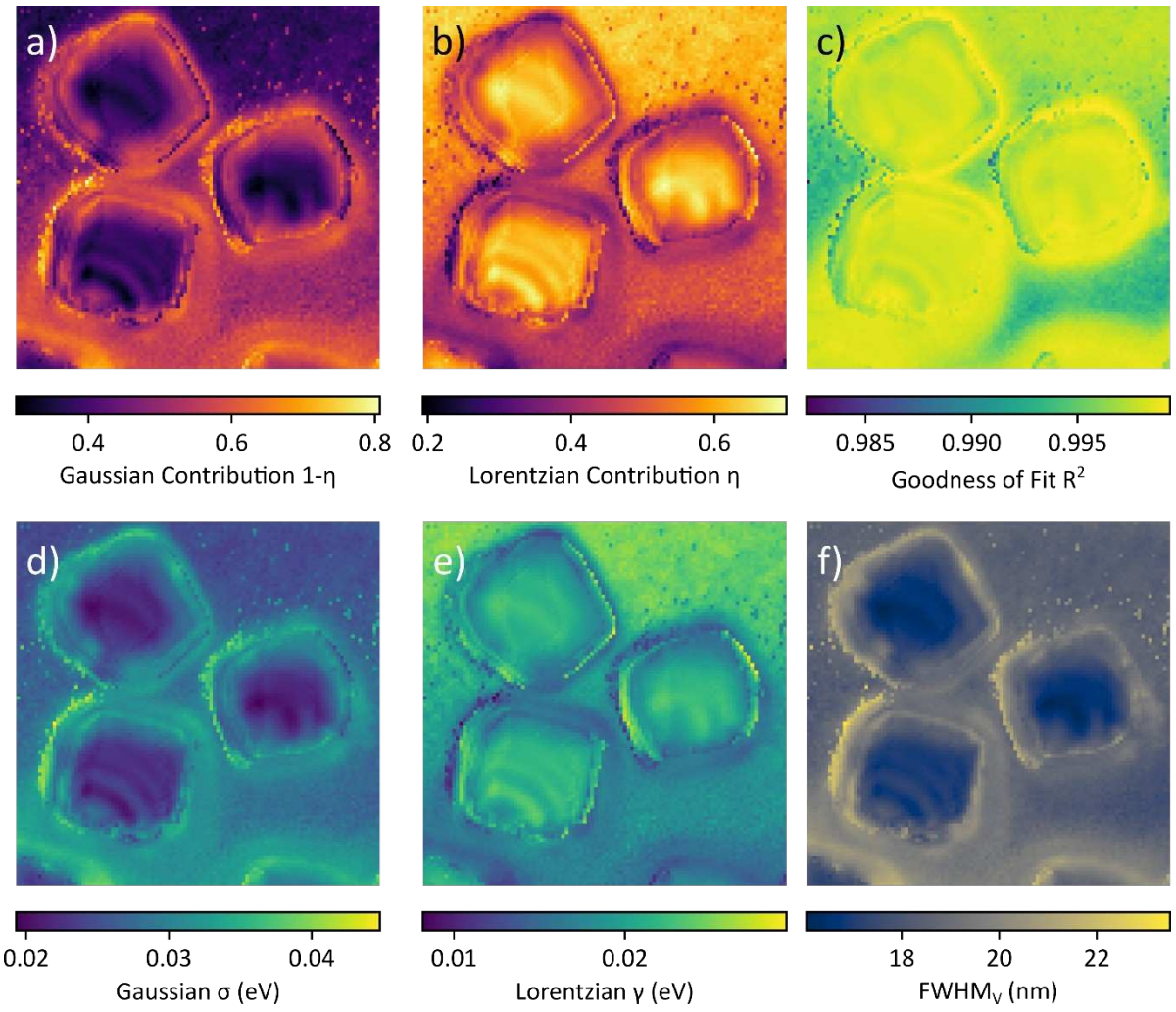

Figure S15. Maps of the PL lineshape parameters extracted from Voigt profiles fitted to all spectra of the spectral map of Fig. 4 of the main text (and Fig. S19). a) Map of the Gaussian contribution to the overall Voigt profile. b) Map of the Lorentzian contribution to the overall Voigt profile. c) Map of the goodness of fit. d) Map of the fitted Gaussian standard deviation. e) Map of the fitted Lorentzian half-width at half-maximum. f) Map of the total fwhm of the fitted Voigt profile.

The maps confirm that the SC edges and the surrounding halo region display the highest Gaussian contribution and largest σ values. This is consistent with a pronounced inhomogeneous broadening in these regions

displaying blue-shifted emission. The goodness of fit of $R^2 > 0.98$ for all pixels confirms the reliability of the Voigt analysis.

5.4 Time-Correlated Single Photon Counting

Fig. S16a) displays the fitting of the overall PL decay data recorded from a 30x30 µm^2 area of a sample consisting of $CsPbBr_3$ SCs embedded in a thin film of NCs on a Si wafer. The map of the amplitude-weighted lifetime in b) is calculated from the fitting parameters obtained from pixel-by-pixel biexponential tailfitting of the TCSPC data. The upper left region of the lifetime map is displayed in Fig. 5e) of the main text.

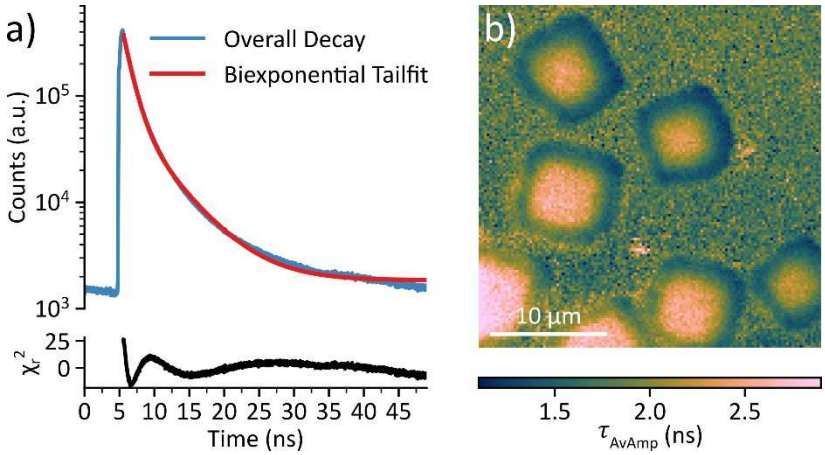

Figure S16. a) Tailfitting of the overall PL decay in the scanned area using a biexponential decay function. The black curve displays the weighted residual χ_r^2. b) Map of the amplitude-weighted average lifetime.

References

(1) Maes, J.; Balcaen, L.; Drijvers, E.; Zhao, Q.; De Roo, J.; Vantomme, A.; Vanhaecke, F.; Geiregat, P.; Hens, Z. Light Absorption Coefficient of $CsPbBr_3$ Perovskite Nanocrystals. *J. Phys. Chem. Lett.* **2018**, *9* (11), 3093–3097. https://doi.org/10.1021/acs.jpclett.8b01065.

(2) Hiller, J. L.; Thalwitzer, R.; Bozkurt, A.; Ferreira, M. G.; Hodak, R.; Strauß, F.; Nadler, E.; Hinsley, G. N.; Wang, B.; Ngoi, K. H.; Rudzinski, W.; Kneschaurek, E.; Roseker, W.; Sprung, M.; Lapkin, D.; Baranov, D.; Schreiber, F.; Vartanyants, I. A.; Scheele, M.; Zaluzhnyy, I. A. Mechanically Robust Supercrystals from Antisolvent-Induced Assembly of Perovskite Nanocrystals. *ACS Nano* **2025**, *19* (28), 26117–26126. https://doi.org/10.1021/acsnano.5c07289.

(3) Ravi, V. K.; Santra, P. K.; Joshi, N.; Chugh, J.; Singh, S. K.; Rensmo, H.; Ghosh, P.; Nag, A. Origin of the Substitution Mechanism for the Binding of Organic Ligands on the Surface of $CsPbBr_3$ Perovskite Nanocubes. *J. Phys. Chem. Lett.* **2017**, *8* (20), 4988–4994. https://doi.org/10.1021/acs.jpclett.7b02192.

(4) De Roo, J.; Ibáñez, M.; Geiregat, P.; Nedelcu, G.; Walravens, W.; Maes, J.; Martins, J. C.; Van Driessche, I.; Kovalenko, M. V.; Hens, Z. Highly Dynamic Ligand Binding and Light Absorption Coefficient of Cesium Lead Bromide Perovskite Nanocrystals. *ACS Nano* **2016**, *10* (2), 2071–2081. https://doi.org/10.1021/acsnano.5b06295.
(5) Toso, S.; Baranov, D.; Altamura, D.; Scattarella, F.; Dahl, J.; Wang, X.; Marras, S.; Alivisatos, A. P.; Singer, A.; Giannini, C.; Manna, L. Multilayer Diffraction Reveals That Colloidal Superlattices Approach the Structural Perfection of Single Crystals. *ACS Nano* **2021**, *15* (4), 6243–6256. https://doi.org/10.1021/acsnano.0c08929.
(6) Toso, S.; Baranov, D.; Giannini, C.; Marras, S.; Manna, L. Wide-Angle X-Ray Diffraction Evidence of Structural Coherence in $CsPbBr_3$ Nanocrystal Superlattices. *ACS Mater. Lett.* **2019**, *1* (2), 272–276. https://doi.org/10.1021/acsmaterialslett.9b00217.
(7) Swarnkar, A.; Marshall, A. R.; Sanehira, E. M.; Chernomordik, B. D.; Moore, D. T.; Christians, J. A.; Chakrabarti, T.; Luther, J. M. Quantum Dot–Induced Phase Stabilization of α-$CsPbI_3$ Perovskite for High-Efficiency Photovoltaics. *Science* **2016**, *354* (6308), 92–95. https://doi.org/10.1126/science.aag2700.
(8) Protesescu, L.; Yakunin, S.; Bodnarchuk, M. I.; Krieg, F.; Caputo, R.; Hendon, C. H.; Yang, R. X.; Walsh, A.; Kovalenko, M. V. Nanocrystals of Cesium Lead Halide Perovskites ($CsPbX_3$, X = Cl, Br, and I): Novel Optoelectronic Materials Showing Bright Emission with Wide Color Gamut. *Nano Lett.* **2015**, *15* (6), 3692–3696. https://doi.org/10.1021/nl5048779.
(9) Eperon, G. E.; Paternò, G. M.; Sutton, R. J.; Zampetti, A.; Haghighirad, A. A.; Cacialli, F.; Snaith, H. J. Inorganic Caesium Lead Iodide Perovskite Solar Cells. *J. Mater. Chem. A* **2015**, *3* (39), 19688–19695. https://doi.org/10.1039/C5TA06398A.
(10) Snare, M. J.; Treloar, F. E.; Ghiggino, K. P.; Thistlethwaite, P. J. The Photophysics of Rhodamine B. *J. Photochem.* **1982**, *18* (4), 335–346. https://doi.org/10.1016/0047-2670(82)87023-8.
(11) Olivero, J. J.; Longbothum, R. L. Empirical Fits to the Voigt Line Width: A Brief Review. *J. Quant. Spectrosc. Radiat. Transf.* **1977**, *17* (2), 233–236. https://doi.org/10.1016/0022-4073(77)90161-3.
(12) Thompson, P.; Cox, D. E.; Hastings, J. B. Rietveld Refinement of Debye–Scherrer Synchrotron X-Ray Data from Al_2O_3. *J. Appl. Crystallogr.* **1987**, *20* (2), 79–83. https://doi.org/10.1107/S0021889887087090.